Composites: Part A 99 (2017) 1–14

Contents lists available at ScienceDirect

Composites: Part A

journal homepage: www.elsevier.com/locate/compositesa

Permeability of textile fabrics with spherical inclusions

Baris Caglar [a,b], Laurent Orgéas [c], Sabine Rolland du Roscoat [c], E. Murat Sozer [a], Véronique Michaud [b,*]

[a] Koc University, Mechanical Engineering Department, Rumelifeneri Yolu, Sariyer 34450, Istanbul, Turkey
[b] Laboratory for Processing of Advanced Composites (LPAC), Ecole Polytechnique Fédérale de Lausanne (EPFL), Station 12, Lausanne CH-1015, Switzerland
[c] CNRS, Univ. Grenoble Alpes, 3SR Lab, F-38000 Grenoble, France

ARTICLE INFO

Article history:
Received 31 December 2016
Received in revised form 9 March 2017
Accepted 26 March 2017
Available online 28 March 2017

Keywords:
A. Fabrics/textiles
B. Permeability
D. Microstructural analysis
E. Liquid Composite Molding

ABSTRACT

We investigated the effect of rigid spherical inclusions such as microcapsules and fillers on the permeability of fabrics by using glass beads as model inclusions. Beads with a range of diameters (40–800 μm) and volume fractions (2.5–10%) were sieved between layers of woven E-glass fabric targeting a fiber volume fraction of 40%. Permeability measurements were completed by X-ray microtomography to analyze the samples pore structure and estimate their permeability using Computational Fluid Dynamics simulations. Experimental and numerical estimates were also fitted with a Kozeny model accounting for porosity and specific surface of samples. We identified a threshold curve related to bead diameter and volume fraction below which the permeability follows that of a plain packed textile, and above which a strong departure from this trend is observed, induced by strong distortions of the textile. This behavior was closely correlated to the internal features of the textile.

1. Introduction

Fiber-Reinforced Polymer Composites (FRPCs) are extensively used in aerospace, automotive, sports and other applications due to their high strength, stiffness and light weight. These materials traditionally consist of a fibrous reinforcement and a polymer matrix. In some cases, a second solid phase, generally in the form of granular particles, may be introduced. As an example, reactive or non-reactive binders (or tackifiers) are introduced at the preforming stage to ease the handling of multiple layers of reinforcement and improve the efficiency of processing [1,2]. Particles may also be integrated to the polymer matrix to improve the mechanical, thermal and electrical properties of the resulting composite [3–7]. In addition, for composite functionalization, self-healing capsules are sieved between the layers of reinforcement [8,9], hollow microspheres are introduced to improve the buoyancy or to produce lightweight parts [10,11], and powders are added to tailor capillary effects in porous structures [12].

The effect of the presence of a second solid phase on the resulting mechanical properties of FRPCs has been extensively investigated and reported in the literature [2,3,8–10,13–18]. It is also well known that the presence of additional solid phases in FRPCs alter the manufacturing processes. For instance, in Liquid Composite Molding (LCM) processes, where a fibrous preform is compacted in a mold and resin is injected into the preform, the preform should be fully impregnated before resin gelation [19]. Hence, an accurate estimate of the permeability of a fibrous structure is essential to predict the flow kinetics and mold filling time [20–23]. Introducing particles directly in the flowing fluid has been reported to increase its viscosity but also to lead to progressive clogging of the particles during processing which results in spatially varying permeability [24–26]. Flow is either modeled by coupling the resin flow with particle filtration by a retention function [27–30] or by simulating the solid-liquid interaction at individual particle level [31–33].

In the case of functionalization by introducing a second solid phase between the layers of fabric, both in-plane and out-of-plane permeability are influenced. Shih and Lee [34] studied the tackification of carbon fiber woven fabrics and used PT 500 binder from 3 M with various binder sizes between 25 μm and 1000 μm. They noted that smaller powders led to a better coverage of the fabric surface and showed that holding the preforms at temperatures higher than the melting temperature of the binder resulted in an increase of the in-plane permeability. In agreement with Rohatgi and Lee [35], they attributed the increase of permeability by the shrinkage of fiber tows following the penetration of molten binder, resulting in larger channels outside the fiber tows. Both studies showed that if the system was held at low temperatures, the binder stayed between the fiber tows and caused a decrease of permeability at high binder concentrations. Estrada et al. [36] investigated the binder influence by modeling the flow in unit cells obtained from micrographs of cut specimens. The unit cell based

* Corresponding author.
E-mail address: veronique.michaud@epfl.ch (V. Michaud).

http://dx.doi.org/10.1016/j.compositesa.2017.03.031
1359-835X/

model showed indeed a different permeability in the principal directions of the anisotropic fabric, but was limited in its predictions as the selected grid was coarse, and the binder distribution was varying a lot. Recently, Becker and Mitschang [37] investigated the influence of preforming technologies (sewing, binder application, shearing and pre-compaction) on the out-of-plane permeability. They reported that the out-of-plane permeability of a glass fiber woven fabric decreased by addition of both activated and non-activated binders. Results showed a lower permeability with activated binder since they caused a more homogenous reduction of available space while non- activated binders hindered nesting, thus leaving some flow channels available. In another study [38], they measured the out-of-plane permeability of preforms manufactured by dry fiber placement, which exhibit one to two orders of magnitude lower out-of-plane permeability than conventional fabrics and they investigated the potential strategies to enhance the out-of-plane permeability of these preforms. They evaluated the effect of binder particle size by sieving three different particle size ranges: medium sized (125–250 μm), coarse (>250 μm) and mixed (in delivery condition) at the same concentration. Highest permeability was observed with the medium sized particles; coarse binders were expected to result in a higher permeability by impeding nesting, but as a lower number of binder particles was introduced to reach the same concentration, the positive effect of sieving large particles was hence reduced. They also studied the influence of binder concentration by sieving different amounts of mixed binders and reported that a slight increase was observed with increasing binder concentration, but positive effects of preserved flow channels were counteracted by blockage of resin flow at high concentrations.

Contrary to the binders whose effect on permeability and microstructure depends on the degree of melting, particle size and concentration, self-healing capsules are rigid inclusions. Manfredi and Michaud [39] investigated the influence of capsule concentration on in-plane permeability by sieving capsules with a size of 125–250 μm. They reported an increase of permeability by addition of self-healing capsules in comparison to samples with no capsules, but without a correlation between capsule concentration and permeability. In the present work, we propose to address, with the use of a model system, the effect of a rigid dispersed second phase in terms of content and granulometry on both the porous structure topology and permeability to develop general guidelines and constitutive models to optimize flow kinetics, a feature which lacked in the aforementioned studies on composite processing.

We thus introduced spherical glass beads with a range of bead volume fractions and diameters into a woven glass fabric. The 3D porous structure of the reinforcements and the role of the beads were finely characterized using X-ray microtomography. In parallel, the in-plane permeability of the reinforcements was estimated using both in-plane permeability experiments and pore-scale Computational Fluid Dynamics (CFD) simulations using the scanned volumes from microtomography analysis. Guidelines were then provided to assess the effect of inclusion size and inclusion volume fraction on the textile permeability, as a function of the microstructural features of the textile.

2. Materials and methods

2.1. Materials

A 2 × 2 twill weave E-glass fabric (Suter Kunststoffe AG) with a nominal areal weight, $g_f = 390$ g/m^2 and a fiber specific mass, $\rho_f = 2.60$ g/cm^3 was used in this study. The fabric was made of fibers with a diameter of 9 μm and consisted of 6 ends/cm along the warp direction and 6.7 picks/cm along the weft direction with 340 and 272 tex, respectively. Rounded glass beads (Microbeads AG, minimum roundness of 0.90) with specific mass, $\rho_b = 2.45$ g/cm^3 were used as model inclusions. As summarized in Table 1, various bead diameter ranges, d_b, were used (40–70, 70–100, 100–200, 200–300, 300–400, and 400–800 μm), as well as various bead volume fractions, ϕ_b (2.5, 5.0 and 10%). Fig. 1a and b shows two typical micrographs corresponding to the 40–70 and 100–200 μm beads. The bead-diameter distributions in Fig. 1c were calculated from the micrographs using the Matlab function *imfindcircles* (~7600 beads were examined under a microscope for 40–70 μm range, and similarly ~4200 beads for 100–200 μm range).

The samples consisted of $n = 8$ layers of fabrics. During sample preparation, the prescribed mass, m_b, of beads was manually sieved between adjacent layers and the resulting stack was then compacted in a mold of volume V_m and thickness $h = 3$ mm. The volume fractions of fibers ϕ_f, of beads ϕ_b, as well as the porosity ϕ_p of processed samples could thus be estimated as $\phi_f = (ng_f)/(h\rho_f) = 40.0 \pm 0.1\%$, $\phi_b = m_b/(\rho_b V_m)$, and $\phi_p = 1 - \phi_f - \phi_b$ (see Table 1). For the permeability experiments, samples had rectangular in-plane dimensions, *i.e.*, 260 mm along the weft direction (the direction along which the permeability was measured, see below) and 60 mm along the warp direction. For X-ray microtomography analysis (see below), the in-plane shape of samples was circular with a 40 mm diameter.

To characterize the permeability of the samples, a solution of polyethylene glycol (PEG, Sigma Aldrich, 35,000 M) was diluted in distilled water with a concentration of 5.7 mmol l^{-1} to form

Table 1
Experimental, numerical and normalized permeability, and specific surface results.

Sample #	Bead properties		Permeability, K [10^{-11} m^2]		Specific surface, S [10^3 m^{-1}]	Normalized permeability, K^*		
	Bead Diameter, d_b (μm)	Bead Volume Fraction, ϕ_b (%)	Experiment, K_{exp}	Simulation, K_{num}		Experiment, K^*_{exp}	Simulation, K^*_{num}	Semi-analytical, K^*_S
1	0	0	7.92	12.2	6.31	1.00	1.00	1.00
2	40–70	2.5	6.50	11.4	5.98	0.82	0.93	0.98
3		5.0	4.04	5.77	8.05	0.51	0.47	0.47
4		10	1.86	4.29	10.1	0.23	0.35	0.23
5	70–100	5.0	3.71	6.78	7.32	0.47	0.56	0.57
6	100–200	2.5	4.96	9.70	6.20	0.63	0.80	0.91
7		5.0	3.89	7.29	7.01	0.49	0.60	0.62
8		10	3.01	5.40	7.22	0.38	0.44	0.44
9	200–300	5.0	5.65	10.6	6.05	0.71	0.87	0.84
10	300–400	5.0	5.94	10.6	5.67	0.75	0.87	0.95
11	400–800	2.5	6.05	12.2	5.78	0.76	1.00	1.05
12		5.0	6.50	13.3	5.62	0.82	1.09	0.97
13		10	6.84	12.1	5.01	0.86	0.99	0.92

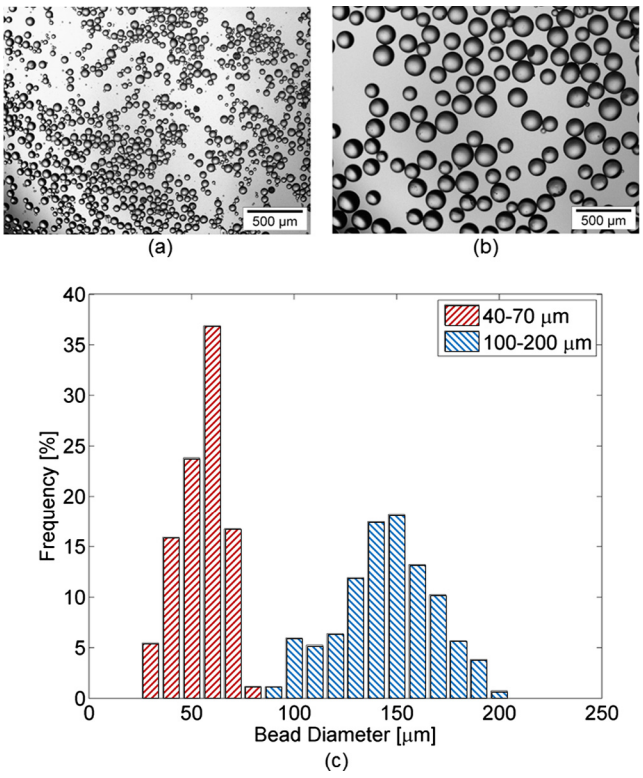

Fig. 1. Optical micrographs of beads with two different diameters, d_b ranges: (a) 40–70 μm, (b) 100–200 μm. (c) Corresponding diameter distribution of the beads. (For interpretation of the references to colour in this figure legend, the reader is referred to the web version of this article.)

the test fluid. The shear viscosity μ of the PEG solution was measured using a Couette rheometer (AR 2000ex, TA Instruments) in continuous flow mode. For characterization of temperature dependency between 18 °C and 25 °C, temperature was increased with a ramp of 0.1 °C min^{-1} and viscosity was measured at a constant shear rate of 1 s^{-1}. For shear rate dependency between 0.1 s^{-1} and 100 s^{-1}, the viscosity was measured at a constant temperature of 20 °C. The PEG solution exhibited a Newtonian behavior as illustrated in Fig. 2 in which the shear viscosity μ *versus* temperature and shear rate was plotted.

2.2. Permeability experiments

Permeability measurements along the weft direction of the fabrics were conducted under constant injection pressure using the mold illustrated in Fig. 3a and b. The guidelines proposed in a recent round-robin study for 1D flow was followed [21] except that a different test-fluid was used. The saturated permeability, denoted as K_{exp}, was measured in all experiments using the injection pressure, p, as well as the temperature of the test fluid, recorded by a Keller S35X piezoresistive transmitter (0–10 bar, 0.02 bar accuracy for pressure, −20 to 150 °C, 0.05% relative accuracy for temperature) placed between the pressure pot and resin inlet. A Mettler Toledo PM2500 scale was placed at the exit to record the mass with an accuracy of 0.001 g at a data acquisition rate of 8 Hz. Mass flow rate was calculated using the acquired mass and time data; additionally, the density of resin was used for calculating the volumetric flow rate, Q. Absence of bead wash-out was ensured by (i) tracking the fluid in the exit tube to observe if there was any bead flowing with the test fluid and (ii) confirming the constant value of mass flow rate over time which would fluctuate in the presence of bead movement. The saturated permeability was then calculated as

$$K_{exp} = (Q\mu L)/(A_c \Delta p) \quad (1)$$

where L is the specimen length along the flow direction (260 mm), A_c is its cross-sectional area (60 mm × 3 mm) and ΔP is the pressure drop between the inlet and exit and is equal to injection pressure p in this case, as the sensor is calibrated to indicate 0 at atmospheric pressure.

In order to determine the permeability of the plain fabric (without beads) for a range of fiber volume fractions, the experiments

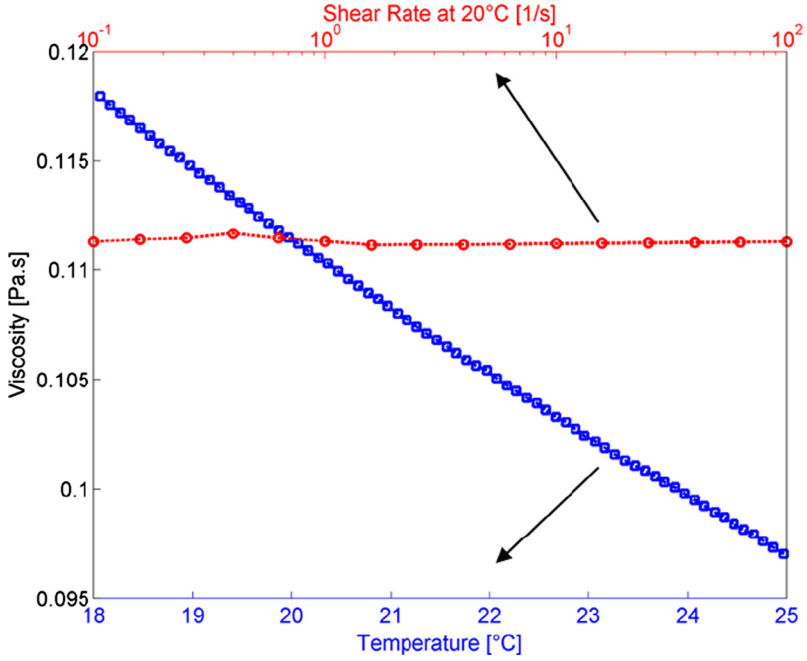

Fig. 2. Shear viscosity μ of the tested PEG solution as a function of temperature (blue curve) and shear rate (red curve). (For interpretation of the references to colour in this figure legend, the reader is referred to the web version of this article.)

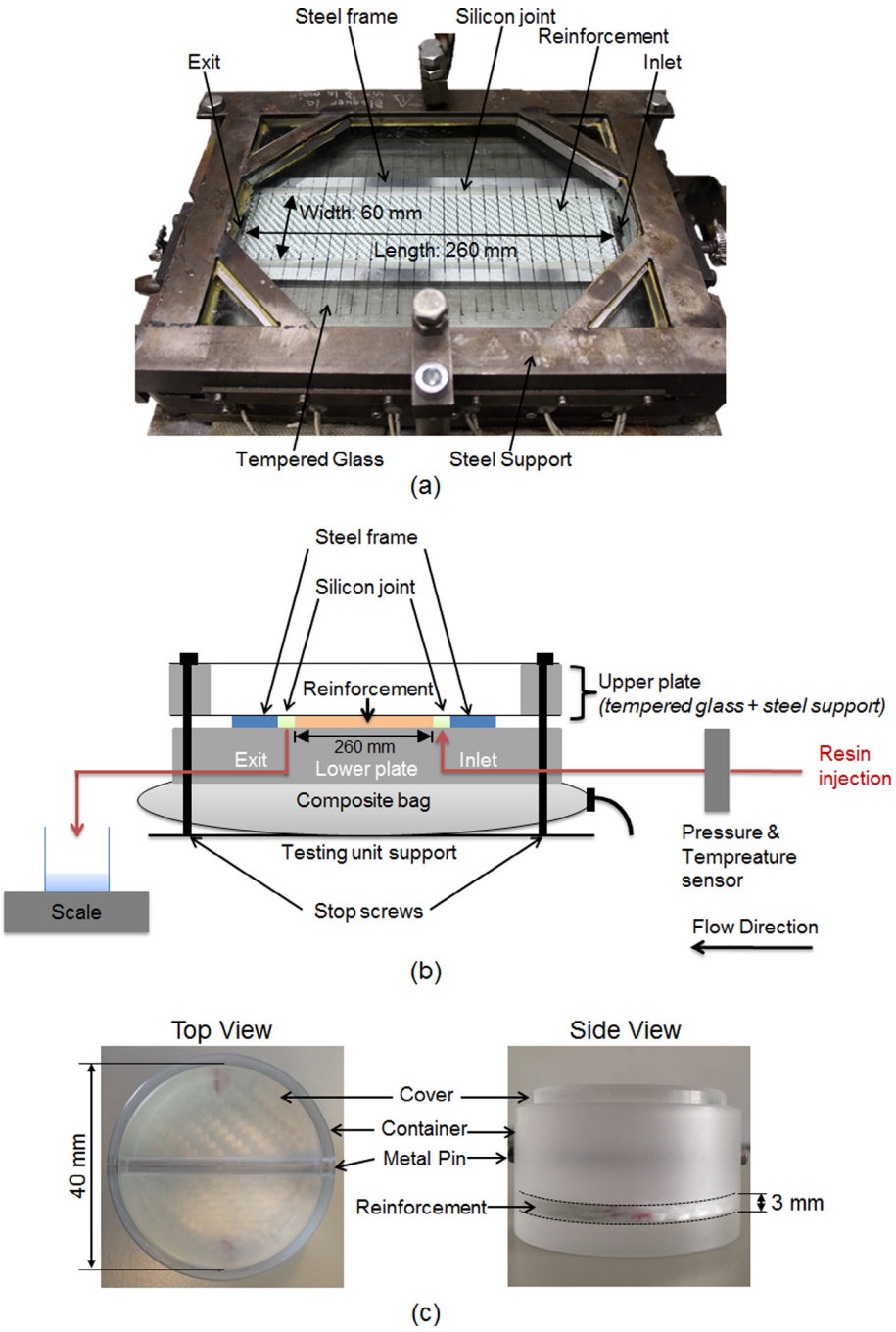

Fig. 3. (a) Experimental setup used for permeability measurements, (b) schematic of the experimental permeability measurement setup, (c) an X-ray microtomography sample. (For interpretation of the references to colour in this figure legend, the reader is referred to the web version of this article.)

initially conducted at $h = 3.0$ mm were also carried out at $h = 2.8$ and 2.5 mm, and the following empirical exponential relation between K_{exp} and ϕ_f (a first order polynomial relation between $\ln K_{exp}$ and ϕ_f) was fitted to the experimental data

$$K_{exp} = Ae^{-b\phi_f} \tag{2}$$

by a least-square method to determine the constants A and b.

2.3. X-ray microtomography

2.3.1. Image acquisition

Cylindrical fabric samples with a diameter of 40 mm were prepared for all configurations listed in Table 1, inserted into cylindrical PMMA containers and compacted to the same thickness, h, of 3 mm as in the permeability experiments, with help of cylindrical PMMA covers held in place with pins (see Fig. 3c). The samples' microstructures were characterized using a laboratory X-ray microtomograph (RX Solutions, 3SR Lab, Grenoble, France). To acquire the 2500 radiographs of size 1840 × 1456 pixels during the 360° rotation of samples with respect to the X-ray source, the generator voltage and the current intensity were set to 120 kV and 83 μA, respectively. After suitable reconstruction, filtering and smoothing operations, 3D greyscale images of the sample absorption coefficients were obtained with a voxel size of $9.85 \times 9.85 \times 9.85\ \mu m^3$. Regions Of Interests (ROIs) of size 1244 × 1244 × 304 voxels were then extracted and subjected to the image analysis procedure detailed hereafter. Fig. 4 shows small

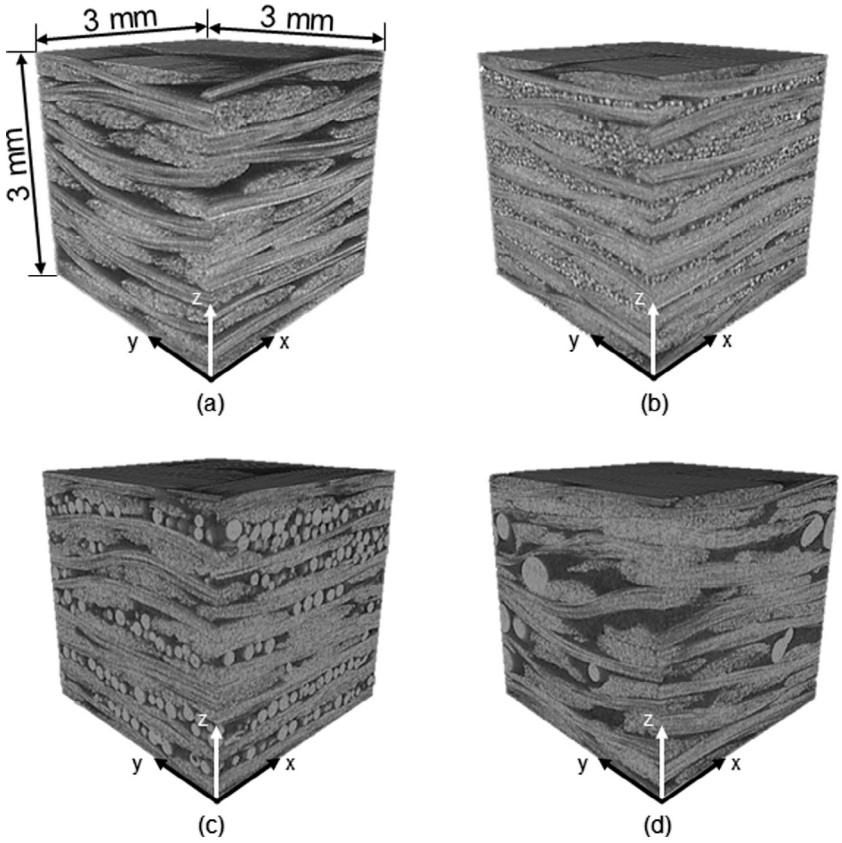

Fig. 4. 3D images (304 × 304 × 304 voxels) showing the structure of (a) a plain sample (*i.e.*, with no beads), and samples with embedded beads with diameters of (b) 40–70 μm, (c) 100–200 μm, and (d) 400–800 μm. Sample thickness, h, in z direction is the same in all samples in (a)–(d); and volume fraction of beads is $\phi_b = 10\%$ in all samples in (b)–(d).

crops (304 × 304 × 304 voxels) achieved inside the reconstructed ROIs to qualitatively illustrate the typical 3D microstructures of four different samples.

2.3.2. Image analysis

In order to assess relevant microstructure descriptors from the scanned samples (see below), the 3D images were first segmented using ImageJ [40] so that the porous phase, the fibers and the beads could be extracted and analyzed independently. The segmentation of the porous phase was readily achieved using a standard thresholding operation due to its strong absorption contrast with respect to the glass fibers and beads. Because of the poor absorption contrast between the beads and the fibers, and additional procedure was needed to extract the beads features from the overall glass phase (see Fig. 5). Thus, in each greyscale slice along the thickness of the imaged samples, *i.e.*, along the z direction, the structure tensor was computed using the plugin FeatureJ of ImageJ [41], and beads were isolated as they exhibited a more isotropic shape than the fibrous network (see Fig. 5b and c). Thereby, additional analyses were conducted:

- The bead segmentation allowed us to locate the beads. Consequently, the normalized z-distribution of the bead content was computed as $\phi^*_{bz} = \phi_{bz}/\phi_b$ where ϕ_b is volume fraction of beads in the entire specimen and ϕ_{bz} is the bead content in each slice parallel to xy plane (*i.e.*, fraction of the slice occupied by the beads). We also built in-plane 2D maps of the bead content ϕ_{bxy}, defined as the volume fraction of beads in the vertical column of height h and cross section area of 1 pixel located at the position (x, y). Thus, ϕ_{bxy} can take a value between 0 and 100% such that $\phi_{bxy} = 100\%$ if all of the 304 slices have a bead at a pixel coordinate of (x, y).
- From the binary image of the porous phase, it was possible to estimate the pore size distribution: (i) by using successive dilation and erosion morphological operations with a cubic structural element; (ii) by counting the remaining voxels after these operations; and (iii) by repeating these operations for increasing sizes of the cubic element [42,43].
- We estimated the mean intercept number of the images, the chord lengths of pores in three principal directions (l_x, l_y, and l_z), their mean values ($\overline{l_x}$, $\overline{l_y}$, and $\overline{l_z}$) as well as the specific surface S of the porous structures, using the method proposed by Rolland du Roscoat et al. [44]. Ratio of mean chord lengths, $r_{xy} = \overline{l_x}/\overline{l_y}$, $r_{xz} = \overline{l_x}/\overline{l_z}$ and $r_{yz} = \overline{l_y}/\overline{l_z}$ were calculated to quantify the anisotropy of the pores. The specific surface S, defined as the surface area of the pore-solid interface per unit volume, is closely linked to the permeability [45]. For example, the following Kozeny equation for unidirectional porous media relates the permeability K to the radius of fibers, R as introduced by Williams et al. [46] and used in composite literature [47,48]:

$$K = \frac{R^2}{4c}\frac{\phi_p^3}{(1-\phi_p)^2} \tag{3}$$

where c is the Kozeny constant. Considering that the porous structure is uniquely made of a network of non-overlapping cylinders of radius R and volume fraction ϕ_f, one gets $S = 2\phi_f/R$ so that:

$$K = \frac{\phi_p^3}{cS^2} \tag{4}$$

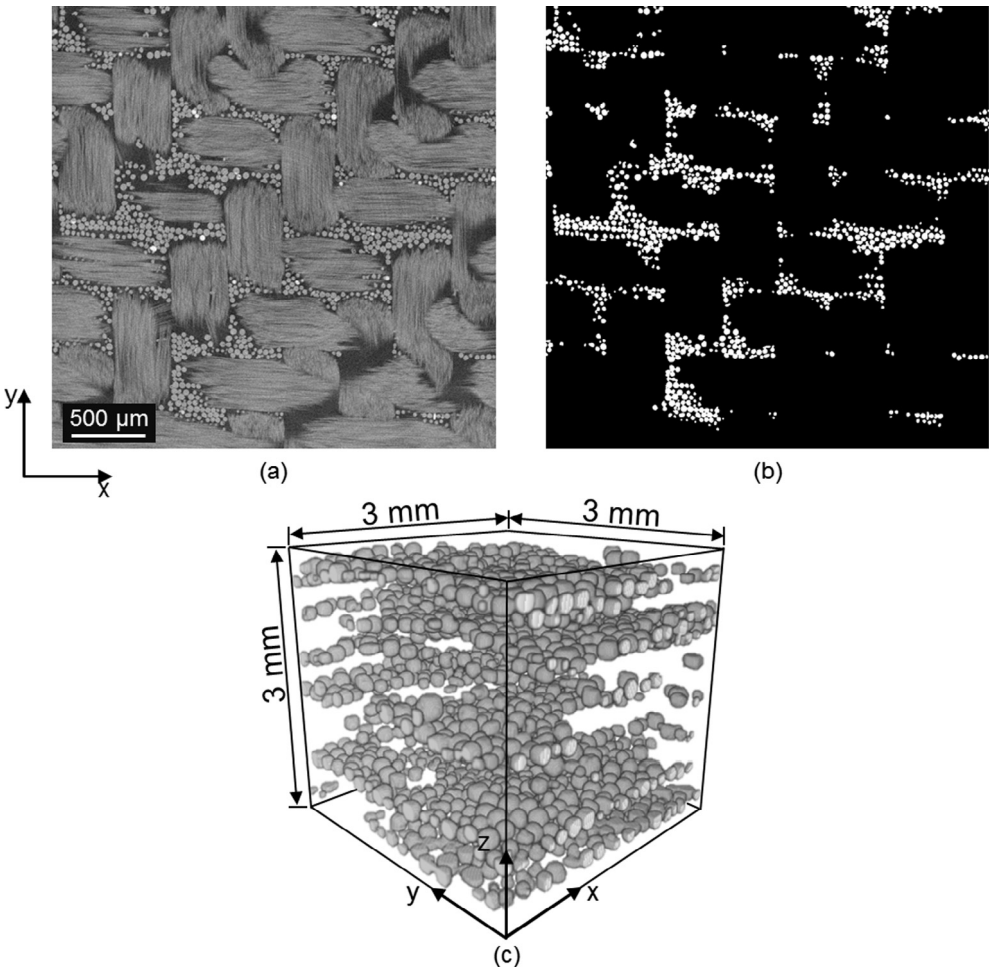

Fig. 5. (a) Slice along thickness direction (*i.e.*, in *xy* plane) of a sample with 100–200 µm beads at ϕ_b = 10%. (b) The beads are seen as white circles after the image treatment of the same slice. (c) 3D volume (304 × 304 × 304 voxels) showing the segmented beads (see Fig. 4c for 3D reconstruction of the original volume).

These equations will be further discussed in Section 3.

2.3.3. Numerical estimation of permeability

The permeability of the samples along the weft direction was also estimated numerically. For these estimations, fluid flow simulations were performed using the commercial Finite Volume software GeoDict [49]. Using the CFD module FlowDict and the Explicit Jump-Stokes (EJ-Stokes) solver, localization Stokes flow problems, deduced from the homogenization method with multiple scale asymptotic expansions [50], were solved within the 3D binary volumes of the pore structures with sizes of 812 × 812 × 304 voxels; the local velocity field as well as the first order pressure fluctuation field were considered as in-plane periodic and the in-plane macroscale pressure-gradient was imposed [51,52].

3. Results and discussion

3.1. Permeability measurements

3.1.1. Experimental results

Experimental values of the textile in-plane permeability $K_{exp,i}$ for each tested sample i (the index $i = 1$ stands for the twill weave) are reported in Fig. 6a and b as a function of porosity and bead diameter, respectively. They have also been gathered in Table 1. The permeability of plain fabrics decreased with increasing ϕ_f, and thus with decreasing ϕ_p, as expected. The parameters of Eq. (2) were found to be $A = 5.99 \times 10^{-8}$ m^2 and $b = 17.2$. Fig. 6a shows that increasing ϕ_b of the smallest beads category (40–70 µm), thus decreasing ϕ_p, had a similar effect on permeability as increasing ϕ_f of the plain fabric. Permeability decreased as ϕ_b increased with a similar trend of the permeability curve as for the plain samples, except for the lowest bead content where the permeability was slightly higher than that recorded for the twill weave at the same volume fraction of solid. Introducing beads with 100–200 µm diameters had a similar effect on permeability and caused an initial decrease in permeability for increasing volume fraction ϕ_b. However, when $\phi_b \geqslant 5.0\%$, the trend for this range of bead diameter diverged from the trend observed with the plain fabrics, the decrease of permeability with decreasing porosity being less pronounced. Surprisingly, for the largest beads (400–800 µm), when $\phi_b \geqslant 2.5\%$, the deviation from the plain fabrics data was significant and such that the permeability even increased when increasing ϕ_b, although the overall porosity decreased. In addition, data plotted in Fig. 6b for $\phi_b = 5.0\%$ shows that the permeability was in the same range for $d_b < 200$ µm (samples #3, #5 and #7), whereas it was significantly higher for $d_b > 200$ µm (samples #9, #10, and #12). These trends suggest that small beads have mainly filled the existing pores while larger ones have deformed the fabric, mainly forming new pores and/or enlarging existing ones.

The relationship between pore size and permeability is detailed in the following sections. A first simple approach can be taken by considering the Hagen-Poiseuille equation ($\Delta P = 8\mu LQ/\pi r^4$), describing the flow in a tube of radius r, which indicates that the

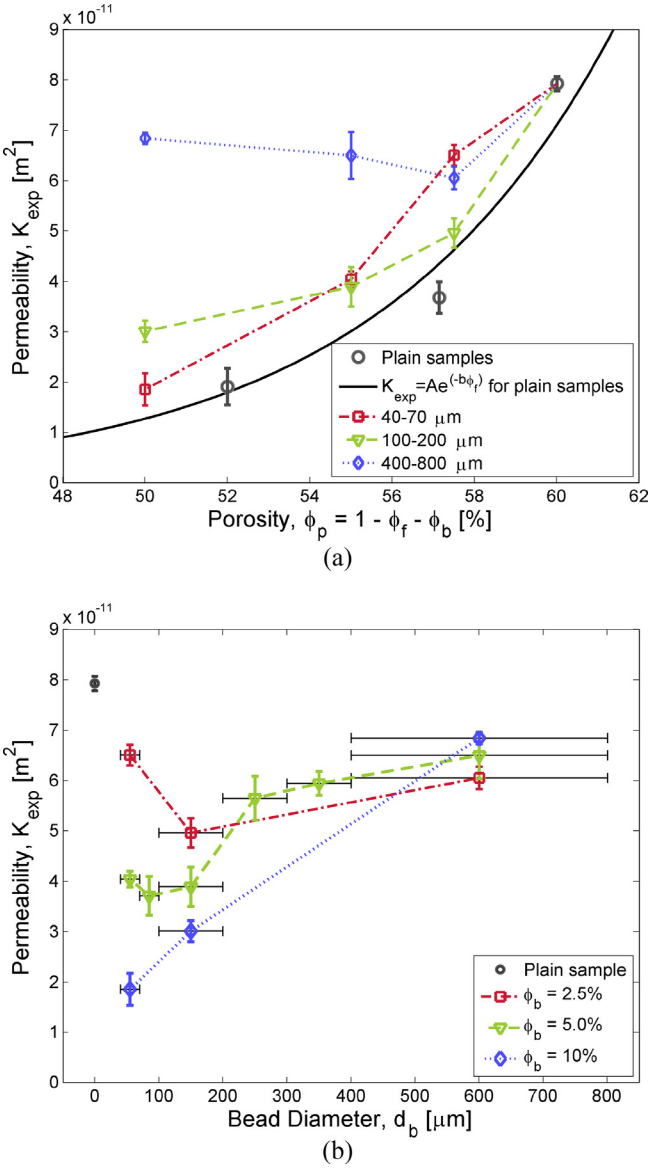

Fig. 6. Textile permeability measured along the weft direction as a function of (a) porosity and (b) bead diameter. In (b), permeability at zero bead diameter corresponds to the permeability of the twill fabric without beads, the horizontal error bars indicate the range of particle size within one type of sample and the vertical error bars are standard deviations in three samples. (For interpretation of the references to colour in this figure legend, the reader is referred to the web version of this article.)

permeability of a simple tube scales with r^2. At equal porosity, a single channel with a large radius should thus provide a higher permeability than multiple channels with a smaller radius. This simple model intuitively explains the higher permeability of samples with large beads compared to the samples with small beads, since the addition of small beads results in the formation of many small channels whereas addition of large beads results in less but larger channels.

3.1.2. Numerical results

Table 1 reports numerical estimations of the permeability $K_{num,i}$ based on the acquired 3D images and pore-scale fluid-flow simulation (see Section 2.3.3). In this table, a single value is reported for each sample, after verifying that chosen size of the representative volume (812 × 812 × 304 voxels) was large enough so that the estimated permeability did not show a significant variation among the volumes cropped from different regions of the full 3D volume (1244 × 1244 × 304 voxels). As seen in Table 1, simulated trends were in good agreement with the experimental results from a qualitative standpoint. However, as already observed for other fibrous structures [53], numerical values were higher than experimental ones: the ratio, K_{num}/K_{exp} ranged between 1.43 and 2.31. Various factors can cause this discrepancy. The two most probable ones may be related to the spatial resolution used for scanning the samples and to the subsequent image analysis operations. Indeed, we chose a voxel size of (9.85 μm)^3 in order to have sufficiently large images with representative volumes of the textiles and beads. However, in doing so, microstructure details lower than the characteristic length of voxels (9.85 μm), such as the fiber scale surface roughness and narrow channels in between fiber bundles or inside fiber bundles, could not be numerically captured very well, although they could significantly contribute to the fluid drag [54,55]. In addition, the filtering and smoothing operations required to delete noise and contributions from other tomography artefacts could have smoothed these microstructural features and thus led to slightly overestimate the permeability. Taking into account these uncertainties, permeability results were normalized in order to provide a suitable quantitative comparison between experimental and numerical results [52,53]. Thus, the following dimensionless experimental $K^*_{exp,i} = K_{exp,i}/K_{exp,1}$ and numerical $K^*_{num,i} = K_{num,i}/K_{num,1}$ permeability were introduced. Here, $K_{exp,1}$ and $K_{num,1}$ denote the experimental and simulated permeability results of the plain sample (i.e., sample #1). As seen in Table 1 and Fig. 7, values of $K^*_{exp,i}$ and $K^*_{num,i}$ were very similar quantitatively, the numerical estimates being slightly higher: both of them captured the effects of the bead content and diameter well.

3.2. Microstructures

3.2.1. Spatial bead distributions

Fig. 8a and b are 2D maps of the bead content ϕ_{bxy} for samples #7 and #13 (see Table 1 for details of samples), respectively. Although the beads were sieved manually, a random bead distribution was achieved when large beads were used (in Fig. 8b), and a quasi-periodic pattern formed when small beads accumulated into the crossing zones of warp/weft bundles (Fig. 8a). These trends are confirmed in Fig. 8c and d, which show the change of ϕ^*_{bz} along the thickness direction of sample #7 (ϕ_b = 5%, d_b = 100–200 μm) and sample #13 ((ϕ_b = 10%, d_b = 400–800 μm)), respectively. In these graphs, the mean values of ϕ^*_{bz} are close to 1 with corresponding ϕ_{bz} being 5.80% and 9.69% respectively, the small deviations being attributed to the fact that only a small section of a sample was analyzed (the overall volume of a sample was $(\pi(20\text{ mm})^2) \times 3\text{ mm} = 3770\text{ mm}^3$ while the evaluated volume was $12\text{ mm} \times 12\text{ mm} \times 3\text{ mm} = 432\text{ mm}^3$). In Fig. 8c, ϕ^*_{bz} varies with a smooth and quasi-periodic oscillatory distribution where seven peaks are observed, which correspond to interlayer spaces within which beads tend to accumulate during the sample fabrication (see also Fig. 4b). On the contrary, in accordance to what is observed in Fig. 8b, such a quasi-periodic distribution is not observed in Fig. 8d. During the fabrication of these samples, the large beads rather deformed the fibrous fabrics, mainly by consolidation but also bending fiber bundles: this is clearly illustrated in Fig. 4d in the case of beads with d_b of 400–800 μm, where fiber bundles are severely bent along the z direction. It should be noted that for all the samples with d_b smaller than 200 μm (samples #2–#8), the distribution of ϕ_b was similar to that of sample #7 showing quasi-periodic in-plane and out-of-plane distributions. In addition, for samples with d_b larger than 200 μm (samples

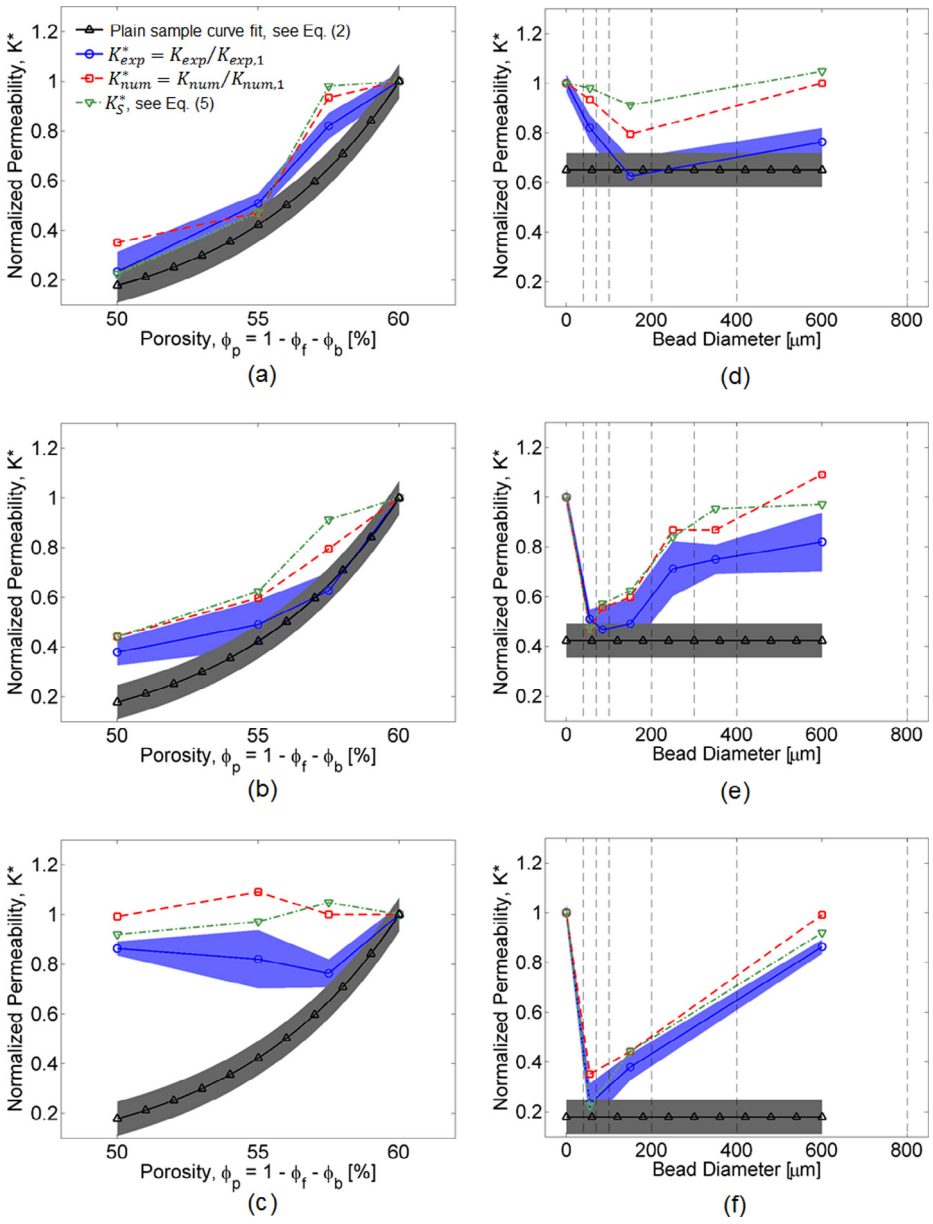

Fig. 7. Normalized permeability as a function of ϕ_p for samples with diameter ranges of 40–70 μm (a), 100–200 μm (b), 400–800 μm (c), and as function of bead diameter for samples with ϕ_b of 2.5% (d), 5.0% (e) and 10% (f). Colored clouds around experimental trends account for the experimental uncertainties. All values are normalized with respect to the results of plain sample with ϕ_p of 60%. (For interpretation of the references to colour in this figure legend, the reader is referred to the web version of this article.)

#9–13), in-plane and out-of-plane distributions were similar to that of sample #13 with a more pronounced deviation from the smooth oscillatory behavior for increasing bead diameter.

3.2.2. Pore size distributions

All results of frequency plots *versus* pore size indicated that, above the resolution of the X-ray Tomograph (9 μm) which did not capture the fiber spacing within tows, the pore size distribution showed a single peak, and only its shape and the magnitude and location of the peak changed. In this case, cumulative pore size distributions are considered more relevant to distinguish the effects, and are plotted for three different d_b ranges (40–70, 100–200, and 400–800 μm) as a function of pore size in Fig. 9a–c (colored curves) along with the pore size distribution of the plain sample (black curve). Fig. 9a reveals that the cumulative frequency increased faster with increasing ϕ_b values so that corresponding curves were skewed towards the left. Though the effect was not very clear for the smallest ϕ_b value of 2.5%, for larger ϕ_b values it is obvious from this graph that large pores present in the plain samples were progressively filled with increasing ϕ_b. In Fig. 9b, a similar trend is observed for samples containing beads with a larger diameter range of 100–200 μm. In Fig. 9c, the opposite trend is observed so that cumulative pore size distribution were skewed towards right with increasing ϕ_b, due to formation of new and larger pores when the embedded beads have d_b = 400–800 μm (see previous subsection).

To better understand the effect of bead diameter on pore size distribution, Fig. 9d–f shows the pore size distribution for the samples with beads at a fixed ϕ_b of 2.5%, 5.0%, and 10%, respectively, along with the pore-size distribution of the plain sample. The pore-size distribution of the samples with ϕ_b of 5.0% in Fig. 9e verifies that sample #9 had a similar pore-size distribution as the

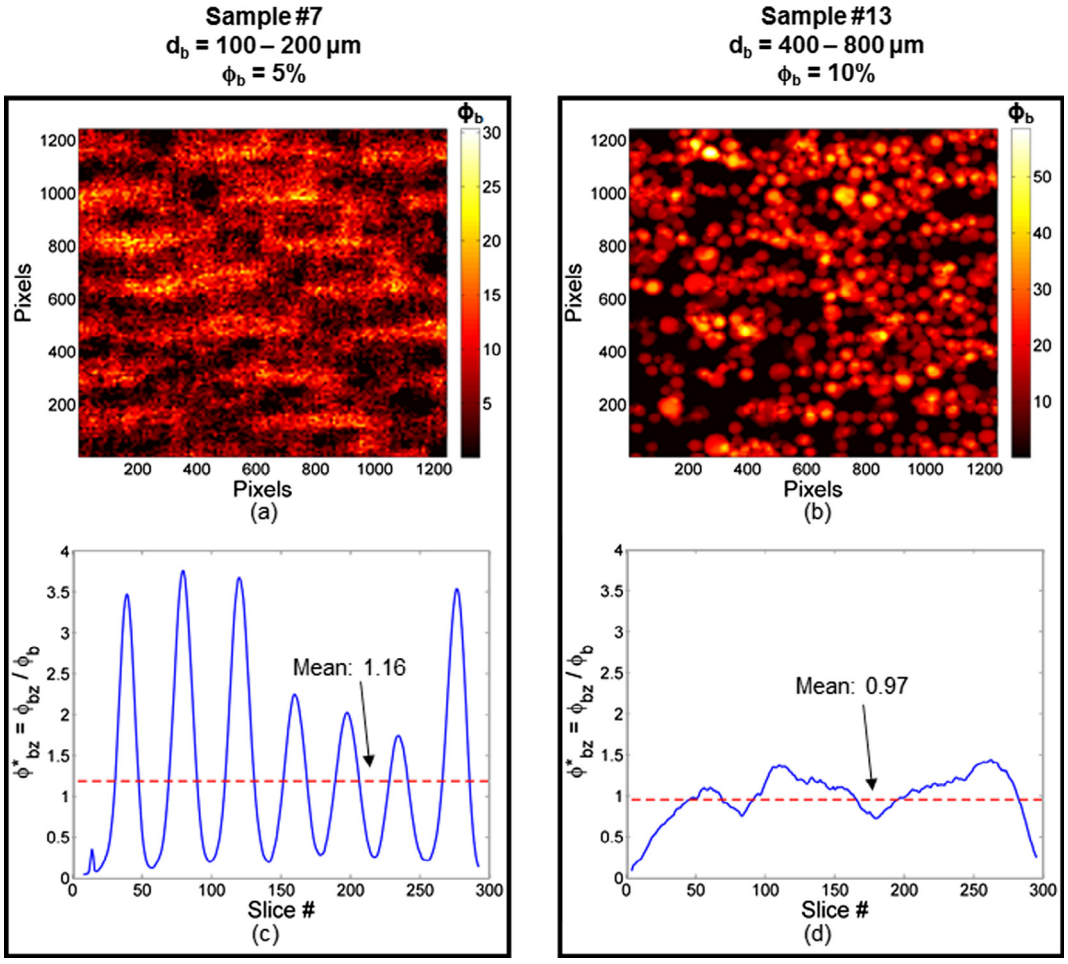

Fig. 8. Analysis of bead distribution in slices along thickness direction, *z*. (a)–(b) Superposed bead distribution at pixels, ϕ_{bxy}, (c)–(d) variation of ϕ^*_{bz} within 304 slices along *z* direction of samples #7 and #13, respectively. Dashed lines in (c) and (d) correspond to the mean ϕ_b values of 5.80% and 9.69%, respectively. (For interpretation of the references to colour in this figure legend, the reader is referred to the web version of this article.)

plain sample (#1), indicating that the embedded beads with $d_b = d_{b,critical}$ = 200–300 µm did not alter the pore-size distribution. This is attributed to an equilibrium between the opposite effects of pore filling by small beads and pore formation by large beads resulting in a completely different topology than the plain sample but with a similar pore size distribution. Beads with $d_b < d_{b,critical}$ and $d_b > d_{b,critical}$ altered the distribution with opposite effects and samples with a bead diameter smaller than 200 µm (samples #3, #5, and #7) had pore size distributions that skewed curves towards left with a more pronounced effect as the bead diameter decreased. In addition, the opposite is true for samples with bead diameter larger than 300 µm (samples #10, and #12) where larger pores were formed by the consolidation and the bending of fiber bundles. Even though only three different diameter-ranges were studied for ϕ_b of 2.5% and 10%, similar behavior in pore-size distributions was observed, *i.e.*, beads with diameter smaller than 200 µm filled the existing pores whereas beads with diameter larger than 300 µm formed larger pores as seen qualitatively in the 3D reconstructions in Fig. 4b–d.

The change in dimensionless permeability reported in Fig. 7d–f directly relates to the aforementioned results. Indeed, at fixed porosity, the permeability is highly affected by the pore space, which is in turn affected by the dimensions of solid (fiber and beads) which make up the porous medium [56–58]: increasing the particle diameter, or more generally shifting the particle size distribution towards larger characteristic lengths usually leads to an increase of the permeability. As shown in Fig. 7d–f, this is in accordance with the results, except for samples with $\phi_b = 2.5\%$ and 5% of the smallest beads. Presumably, particle locations for these samples may have differed from those observed for other beads contents or sizes. Similarly, increasing the bead content for large beads results in a shift towards larger characteristic lengths and an increase of permeability, but with a natural limit as shown by the gradual differences between samples #12 and #13 in Figs. 7c and 9c, respectively.

3.2.3. Pore shape anisotropy

Anisotropy ratios of the mean-pore chord-lengths were calculated, $r_{xy} = \overline{l_x}/\overline{l_y}$, $r_{xz} = \overline{l_x}/\overline{l_z}$ and $r_{yz} = \overline{l_y}/\overline{l_z}$ and plotted as a function of ϕ_b of samples with d_b = 100–200 µm in Fig. 10a and plotted as a function of d_b of samples with ϕ_b = 5.0% in Fig. 10b. Both figures indicate that the pores exhibited flat shapes. The in-plane anisotropy (r_{xy}) of the twill sample without beads, due to inherent difference between the warp and weft directions of the fabric, was reduced by introduction of the beads. In Fig. 10a, increasing ϕ_b resulted in a transition towards more isotropic pores, highlighted by the significant decreases in r_{xz} and r_{yz}. Similar trends were observed among the samples with d_b = 40–70 µm and d_b = 400–800 µm, which were not plotted here for the sake of brevity. In

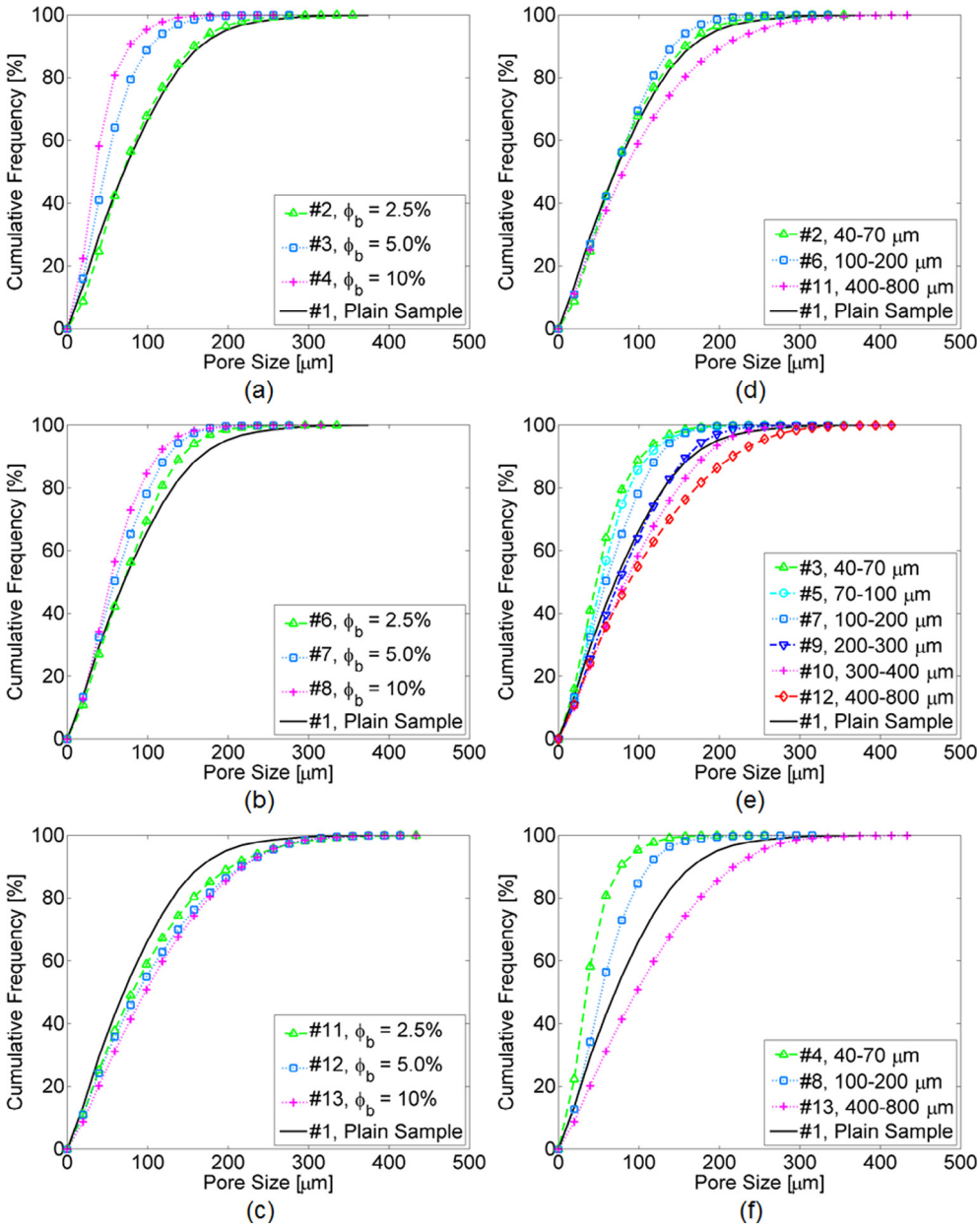

Fig. 9. Cumulative pore size distribution of samples with embedded beads which have a diameter range, d_b, of 40–70 μm (a), 100–200 μm (b), 400–800 μm (c); and a fixed bead-volume-fraction, ϕ_b, of 2.5% (d), 5.0% (e) and 10% (f). Pore size distribution of twill sample alone ($\phi_b = 0$) is included in the plots for comparison. (For interpretation of the references to colour in this figure legend, the reader is referred to the web version of this article.)

Fig. 10b, no clear dependency of anisotropy was observed on d_b, yet all the samples were less anisotropic than the plain sample and same behavior is observed among the samples with $\phi_b = 2.5\%$ and 10%, again not plotted for the sake of brevity.

3.2.4. Specific surface and semi-analytical permeability estimation

Values of the computed specific surface, S, are listed in Table 1. Recall that these values were obtained with a voxel size of $(9.85\ \mu m)^3$, *i.e.*, with a characteristic length close to the fiber radius (9 μm): they can be considered as mesoscale values, well suited for fiber bundles and beads only. For the sample without bead (#13), following the $S = 2\phi_f/R$ relationship, R was evaluated from the measured surface area and was on the order of hundred microns, which is comparable to the geometric mean of the semi-minor and semi-major axes of ideally elliptical fiber bundles. By embedding beads into a fabric preform, values reported in Table 1 prove that the specific surface S of the overall media (fabric preform and beads) exhibited complex trends due to various competing mechanisms:

At a fixed bead diameter, (i) increasing the bead content was prone to increase S. However, at the same time, this could induce (ii) the consolidation of the fiber bundle and thus a decrease of the mesoscale specific surface. As shown in Table 1, mechanism (i) governed the structure of the assemblies at low bead diameters, whereas mechanism (ii) was predominant at higher bead diameters: for samples with bead diameter higher than 100–200 μm, the resulting specific surfaces were even lower than those recorded for the twill weave alone.

At a fixed volume-fraction of solids, (iii) decreasing the bead diameter was also prone to increase the mesoscale specific surface, provided that subsequent consolidation mechanisms of the fiber

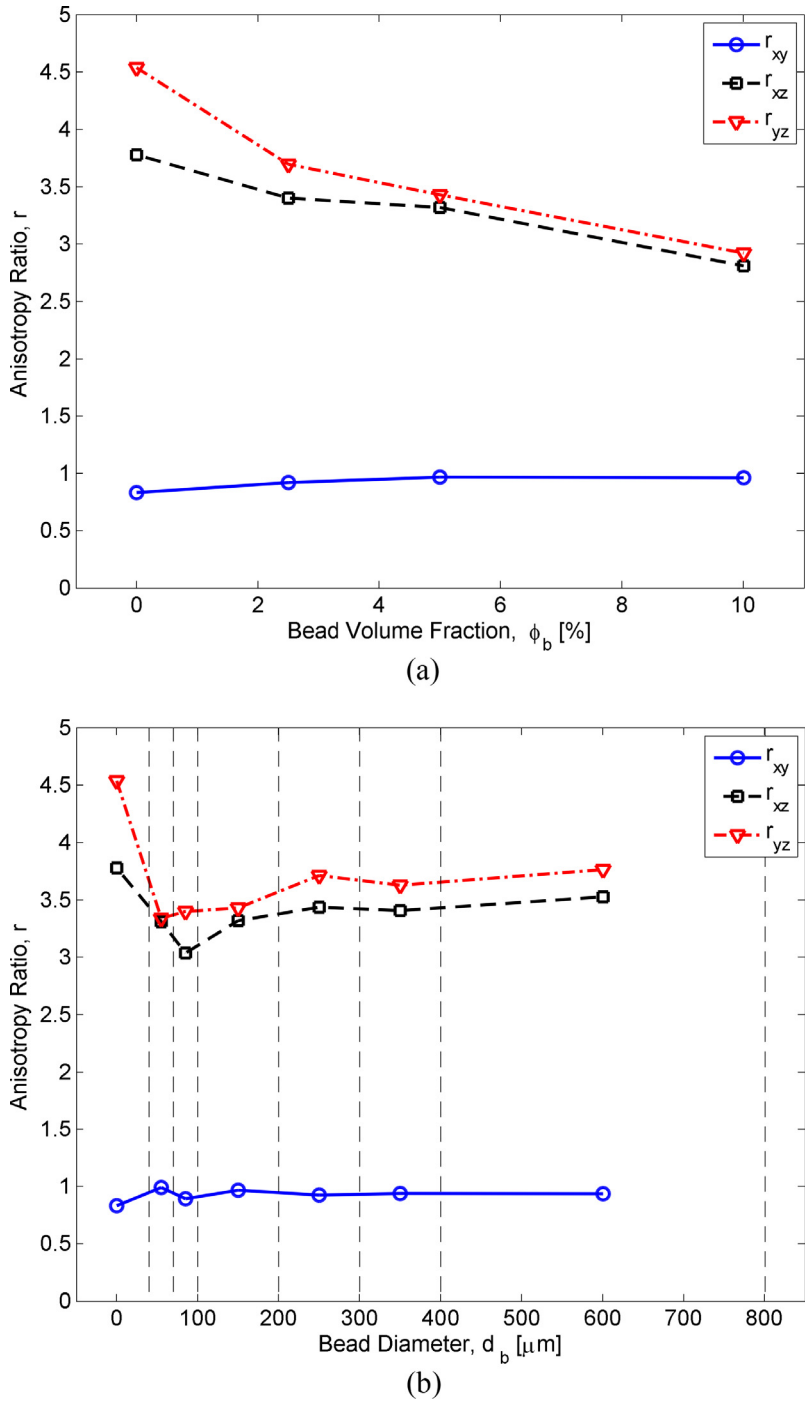

Fig. 10. Anisotropy ratio as a function of bead volume fraction ϕ_b for samples with bead-diameter range of 100–200 μm (a), as a function of bead diameter d_b for samples with bead-volume-fraction of 5.0% (b). In (a), ϕ_b = 0 corresponds to the twill sample alone. In (b), d_b = 0 of d_b of samples with ϕ_b of 5.0% in Fig. 10b. In Fig. 10a, and the vertical dashed lines correspond to the lower and upper bounds for each diameter range. (For interpretation of the references to colour in this figure legend, the reader is referred to the web version of this article.)

bundles were restrained. Table 1 verifies that mechanism (iii) governed the mesostructures of the assemblies for the two highest investigated bead contents. For the lowest investigated bead content, mechanism (iii) seemed to be important above bead diameters of 100–200 μm. Below this diameter range, mechanism (ii) might be predominant.

Lastly, dimensionless semi-analytical permeability values based on S measurements, $K^*_{S,i} = K_{S,i}/K_{S,1}$, were calculated using Eq. (4) as follows

$$K^*_{S,i} = \frac{S_1^2 \phi_i^3}{S_i^2 \phi_1^3} \tag{5}$$

under the assumption that Kozeny constant, c, was equal for all configurations. These estimates are reported in Fig. 7 and Table 1. As obvious from this figure and this table, $K^*_{S,i}$ follow rather closely the trends given both by the experiments ($K^*_{exp,i}$) and the pore scale CFD simulations ($K^*_{num,i}$) and the correlation between $K^*_{S,i}$ and $K^*_{num,i}$

is better as analytical and numerical estimates were obtained from the same volumes. Thus, these results indicate that from a "simple" analytical model and the knowledge of the specific surface of the samples, reliable semi-analytical estimate of $K^*_{S,i}$ can be obtained, emphasizing the role of porosity ϕ_b and specific surface S on the permeability.

3.2.5. Pore chord length and bead diameter relationship

As reported in Figs. 6 and 7 for ϕ_b = 5.0 and 10%, a change in permeability regime occurred at critical bead diameters d_b of ≈100–200, and 40–70 μm, respectively. Above these critical values, the specimens' permeability was higher than that of the twill weave alone at the same volume fraction of solid. This transition was attributed to the extensive deformation of fabric (consolidation and distortion) as large beads were introduced. A similar transition was observed for the pore-size distribution (see Fig. 9d) and bead distribution along the thickness direction (see Fig. 8c and d), the relation between the geometrical characteristics of the fabric and pore diameter and content should be revealed.

An analysis on the smallest chord length of the twill weave without bead, *i.e.*, the out-of-plane pore chord length l_z, showed that (i) the porosity exhibited a strong out-of-plane anisotropy (Fig. 10) and (ii) adding beads into the twill weave mainly resulted in yarn distortion along the z direction (see Fig. 4c and d). The continuous line in Fig. 11 plots the dependence of the cumulative porosity ϕ_{pz} on the out-of-plane chord length l_z. Due to the voxel size used to image the sample $(9.85\ \mu m)^3$, ϕ_{pz} goes from 0 to $\phi_{pz,max} = 35\%$, this value being obviously lower than the overall porosity of the twill weave (60%). However, this difference does not affect the relationship between the pore-size distribution of the mesostructures and the bead diameters, since the smallest of the studied beads has a diameter range of 40–70 μm, which is significantly larger than the voxel size. Thus, for a given value $l_{z,i}$, the corresponding porosity value $\phi_{pz,i}(l_{z,i})$ represents the volume fraction of pores with chord lengths equal to or smaller than $l_{z,i}$. This also means that chords larger than $l_{z,i}$ occupy a porosity of $\phi_{pz,max} - \phi_{pz,i}(l_{z,i})$. Therefore, bearing in mind that pores are highly anisotropic (see Fig. 10), it is reasonable to imagine two possible scenarios when beads with a diameter d_b close to $l_{z,i}$ are added into the twill weave:

(a) They first fill the empty space of porosity $\phi_{pz,max} - \phi_{pz,i}(l_{z,i})$, without causing significant consolidation or bending of fiber bundles (see Fig. 4b). This would be possible as long as the volume content of beads in these pores remains below a critical bead content which we can here approximate, as a first approach, as the maximal random close packing fraction for spherical particles $\phi_{lp} \approx 0.64$ [59].

(b) Above such a bead content, a consolidation of fiber bundles and/or an out-of-plane bending of fiber bundles takes place; the prevalence of one of the two aforementioned mechanisms may occur as follows:
   i. The lower the bead diameter, the higher the bead content to reach regime (b) and the higher the consolidation of the twill weave, as illustrated in the example shown in Fig. 4c.
   ii. Conversely, the higher the bead diameter, the lower the bead content to reach regime (b), and the higher the distortion of the fabrics that result in significant pore opening (Fig. 4c and d).

Fig. 11 reports the values of $d_b, \phi_b/\phi_{lp}$ used in the tested samples, in order to emphasize whether scenarios (a) or (b) (*i.e.*, the points below or above the black curve, respectively) were prone to occur. In addition, the green rectangular points in Fig. 7 indicate that the experimental dimensionless permeability K^*_{exp} of the samples was close to the permeability of the consolidated twill weave without bead, $K^*_{plain}(\phi_f + \phi_b)$. Similarly, red circular points indicate samples whose experimental dimensionless permeability K^*_{exp} was higher than $K^*_{plain}(\phi_f + \phi_b)$. Fig. 11 clearly proves that all samples located above the continuous black curve, *i.e.*, those corresponding to the bead-filling scenario (b), exhibited a higher permeability than the twill weave at the same porosity. In addition, as illustrated in Fig. 4c and d, these samples all exhibited pronounced bundle bending, *i.e.*, following filling mechanisms (b-ii) with pore opening. Consequently, the prevalence of bundle distortion during

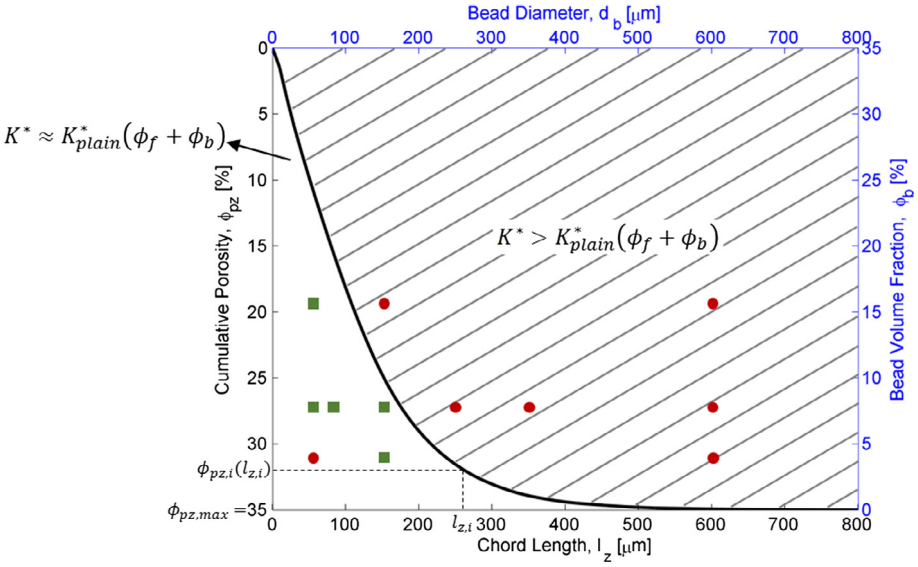

Fig. 11. The black continuous curve represents the cumulated porosity of the twill sample without bead as a function of chord length in z direction l_z, dividing the domain into two regions: in one region $K \approx K_{plain}(\phi_f + \phi_b)$; and in the other region $K > K_{plain}(\phi_f + \phi_b)$. ■ and ● denote the experimentally studied bead diameter and volume fraction combinations, the former classifies the combinations respecting the $K \approx K_{plain}(\phi_f + \phi_b)$ behavior and the latter classifies the rest. (For interpretation of the references to colour in this figure legend, the reader is referred to the web version of this article.)

the filling of the twill weave with adequately big beads induced pore opening and limited the increase of, or even decreased, the sample specific surface. Thus, in spite of the overall decrease of the sample porosity, the decrease in sample permeability was less pronounced than the twill weave alone, or even increased (see Eq. (5)).

In addition, as emphasized in Fig. 11, data located below the continuous black curve correspond to filling scenario (a). It is interesting to notice that at given volume fraction of pores, the permeability of most of them is rather close to that of the fabric without bead (see also Fig. 7). For these situations, filling mechanisms thus resulted in specific-surface changes similar to those encountered during the compaction of the twill weave alone. This general trend is however not fulfilled by the sample at the lowest bead content and diameter; as mentioned previously, the bead placement of this sample might have differed from the other samples during filling.

4. Conclusion

This study investigated the influence of spherical inclusions on textile permeability. For that purpose, we carried out a systematic analysis using a glass twill weave and glass beads with various diameter ranges (40–70, 70–100, 100–200, 200–300, 300–400, and 400–800 μm) and volumetric concentrations (2.5, 5.0 and 10%). The analysis was carried out by combining 3D imaging of the fabric mesostructures (using X-ray microtomography) together with experimental and numerical estimations of fabric in-plane permeability (using a permeability setup and pore scale CFD simulations, respectively). Experimental and numerical results were in good agreement and indicated that the dimensionless permeability was a complex function of the bead content and diameter. For low bead contents and diameters, a permeability decrease was observed with introduction of beads, which mostly followed the trend of the twill weave alone at the same porosity. At a sufficiently large bead diameter, a reversion of this trend was observed.

Pore-size distributions as well as specific-surface estimations were in agreement with experimental and numerical permeability estimations, showing that the in-plane permeability was a function of two competing mechanisms, namely pore filling (mostly in the case of small beads) and new pore formation and/or pore opening due to fabric distortion (mostly in the case of large beads). In addition, we showed that from the knowledge of the sample porosity and specific surface, together with a Kozeny-like permeability approach, it was possible to give relevant semi-analytical estimates of the dimensionless in-plane permeabilities of the filled fabrics. This could be used for guidelines if one lacks access to experimental or numerical facilities.

Analysis of pore mean chord length inside the 3D images of the samples also showed that both in the absence and in the presence of beads, pore shapes were strongly anisotropic and exhibited flat shapes. The anisotropy was reduced by introduction of the beads, in comparison to the twill sample, especially the anisotropy between in-plane directions. The mean chord length along the thickness direction remained significantly lower than the in-plane values. In addition, critical pairs of parameter (d_b, ϕ_b) were emphasized. Below these critical values, beads mainly fill the fabric without pronounced modification of its mesostructure. Under such circumstances, both the sample specific surface and permeability follow trends of the compacted fabric alone. Above these values, beads induce consolidation and high distortion of the fiber bundles (mainly out-of-plane bending), pore opening, modification of the specific surface towards slight increase or even decrease with respect to what could be expected with the compacted fabric, and thus higher permeability. We also showed that the critical pairs of parameters (d_b, ϕ_b) were closely correlated to the distribution of pore chord lengths of the plain twill weave along its thickness. Thus, a simple analysis of the plain fabric mesostructure is sufficient to construct first estimates of the influence of a given volume fraction and size of inclusions on permeability.

Acknowledgements

This work is supported by Swiss Government Excellence Scholarship Program and the Scientific and Technological Research Council of Turkey (TUBITAK). Damiano Salvatori is gratefully acknowledged for his help in the experimental work.

References

[1] Advani SG, Sozer EM. Process modeling in composites manufacturing 2002;436.
[2] Tanoglu M. Investigating the effects of a polyester preforming binder on the mechanical and ballistic performance of E-glass fiber reinforced polyester composites. Int J Adhes Adhes 2003;23:1–8. http://dx.doi.org/10.1016/S0143-7496(02)00061-1.
[3] Fu S-Y, Feng X-Q, Lauke B, Mai Y-W. Effects of particle size, particle/matrix interface adhesion and particle loading on mechanical properties of particulate–polymer composites. Compos Part B Eng 2008;39:933–61. http://dx.doi.org/10.1016/j.compositesb.2008.01.002.
[4] Lee GW, Park M, Kim J, Lee JI, Yoon HG. Enhanced thermal conductivity of polymer composites filled with hybrid filler. Compos Part A Appl Sci Manuf 2006;37:727–34. http://dx.doi.org/10.1016/j.compositesa.2005.07.006.
[5] Aktas L, Dharmavaram S, Hamidi YK, Cengiz Altan M. Filtration and breakdown of clay clusters during resin transfer molding of nanoclay/glass/epoxy composites. J Compos Mater 2008;42:2209–29. http://dx.doi.org/10.1177/0021998308094556.
[6] Reia Da Costa EF, Skordos AA, Partridge IK, Rezai A. RTM processing and electrical performance of carbon nanotube modified epoxy/fibre composites. Compos Part A Appl Sci Manuf 2012;43:593–602. http://dx.doi.org/10.1016/j.compositesa.2011.12.01.
[7] Chisholm N, Mahfuz H, Rangari VK, Ashfaq A, Jeelani S. Fabrication and mechanical characterization of carbon/SiC-epoxy nanocomposites. Compos Struct 2005;67:115–24. http://dx.doi.org/10.1016/j.compstruct.2004.01.010.
[8] Kessler M, Sottos NR, White S. Self-healing structural composite materials. Compos Part A Appl Sci Manuf 2003;34:743–53. http://dx.doi.org/10.1016/S1359-835X(03)00138-6.
[9] Manfredi E, Cohades A, Richard I, Michaud V. Assessment of solvent capsule-based healing for woven E-glass fibre-reinforced polymers. Smart Mater Struct 2015;24:15019. http://dx.doi.org/10.1088/0964-1726/24/1/015019.
[10] Zhang X, Wang P, Zhou Y, Li X, Yang E-H, Yu TX, et al. The effect of strain rate and filler volume fraction on the mechanical properties of hollow glass microsphere modified polymer. Compos Part B Eng 2016;101:53–63. http://dx.doi.org/10.1016/j.compositesb.2016.06.079.
[11] Porfiri M, Gupta N. Effect of volume fraction and wall thickness on the elastic properties of hollow particle filled composites. Compos Part B Eng 2009;40:166–73. http://dx.doi.org/10.1016/j.compositesb.2008.09.002.
[12] Kostornov AG, Moroz AL, Shapoval AA, Kabov O, Strizhak P, Legros JC. Composite structures with gradient of permeability to be used in heat pipes under microgravity. Acta Astronaut 2015;115:52–7. http://dx.doi.org/10.1016/j.actaastro.2015.04.022.
[13] Tanoglu M, Seyhan AT. Compressive mechanical behaviour of E-glass/polyester composite laminates tailored with a thermoplastic preforming binder. Mater Sci Eng A 2003;363:335–44. http://dx.doi.org/10.1016/j.msea.2003.08.005.
[14] Wu W, Klunker F, Xie L, Jiang B, Ziegmann G. Simultaneous binding and ex situ toughening concept for textile reinforced pCBT composites: Influence of preforming binders on interlaminar fracture properties. Compos Part A Appl Sci Manuf 2013;53:190–203. http://dx.doi.org/10.1016/j.compositesa.2013.06.013.
[15] Hillermeier RW, Seferis JC. Interlayer toughening of resin transfer molding composites. Compos Part A Appl Sci Manuf 2001;32:721–9. http://dx.doi.org/10.1016/S1359-835X(00)00088-9.
[16] Fu S-Y, Lauke B. Fracture resistance of unfilled and calcite-particle-filled ABS composites reinforced by short glass fibers (SGF) under impact load. Compos Part A Appl Sci Manuf 1998;29:631–41. http://dx.doi.org/10.1016/S1359-835X(97)00111-5.
[17] Gupta N, Priya S, Islam R, Ricci W. Characterization of mechanical and electrical properties of epoxy-glass microballoon syntactic composites. Ferroelectrics 2006;345:1–12. http://dx.doi.org/10.1080/00150190601018002.
[18] Wang P, Xu S, Li Z, Yang J, Zheng H, Hu S. Temperature effects on the mechanical behavior of aluminum foam under dynamic loading. Mater Sci Eng A 2014;599:174–9. http://dx.doi.org/10.1016/j.msea.2014.01.076.

[19] Caglar B, Yenilmez B, Sozer EM. Modeling of post-filling stage in vacuum infusion using compaction characterization. J Compos Mater 2015;49:1947–60. http://dx.doi.org/10.1177/0021998314541305.
[20] Loix F, Badel P, Orgéas L, Geindreau C, Boisse P. Woven fabric permeability: from textile deformation to fluid flow mesoscale simulations. Compos Sci Technol 2008;68:1624–30. http://dx.doi.org/10.1016/j.compscitech.2008.02.027.
[21] Arbter R, Beraud JM, Binétruy C, Bizet L, Bréard J, Comas-Cardona S, et al. Experimental determination of the permeability of textiles: a benchmark exercise. Compos Part A Appl Sci Manuf 2011;42:1157–68. http://dx.doi.org/10.1016/j.compositesa.2011.04.021.
[22] Vernet N, Ruiz E, Advani SG, Alms JB, Aubert M, Barburski M, et al. Experimental determination of the permeability of engineering textiles: Benchmark II. Compos Part A Appl Sci Manuf 2014;61:172–84. http://dx.doi.org/10.1016/j.compositesa.2014.02.010.
[23] Di Fratta C, Klunker F, Trochu F, Ermanni P. Characterization of textile permeability as a function of fiber volume content with a single unidirectional injection experiment. Compos Part A Appl Sci Manuf 2015;C:238–47. http://dx.doi.org/10.1016/j.compositesa.2015.05.02.
[24] Nordlund M, Fernberg SP, Lundström TS. Particle deposition mechanisms during processing of advanced composite materials. Compos Part A Appl Sci Manuf 2007;38:2182–93. http://dx.doi.org/10.1016/j.compositesa.2007.06.009.
[25] Garay AC, Heck V, Zattera AJ, Souza Ja, Amico SC. Influence of calcium carbonate on RTM and RTM light processing and properties of molded composites. J Reinf Plast Compos 2011;30:1213–21. http://dx.doi.org/10.1177/0731684411416O3.
[26] Gnidakouong JRN, Roh HD, Kim J, Park Y. In situ assessment of carbon nanotube flow and filtration monitoring through glass fabric using electrical resistance measurement. Compos Part A Appl Sci Manuf 2016;90:137–46. http://dx.doi.org/10.1016/j.compositesa.2016.07.005.
[27] Lefevre D, Comas-Cardona S, Binétruy C, Krawczak P. Modelling the flow of particle-filled resin through a fibrous preform in liquid composite molding technologies. Compos Part A Appl Sci Manuf 2007;38:2154–63. http://dx.doi.org/10.1016/j.compositesa.2007.06.008.
[28] Lefevre D, Comas-Cardona S, Binetruy C, Krawczak P. Coupling filtration and flow during liquid composite molding: experimental investigation and simulation. Compos Sci Technol 2009;69:2127–34. http://dx.doi.org/10.1016/j.compscitech.2009.05.008.
[29] Haji H, Saouab A, Nawab Y. Simulation of coupling filtration and flow in a dual scale fibrous media. Compos Part A Appl Sci Manuf 2015;76:272–80. http://dx.doi.org/10.1016/j.compositesa.2015.06.004.
[30] Reia da Costa EF, Skordos AA. Modelling flow and filtration in liquid composite moulding of nanoparticle loaded thermosets. Compos Sci Technol 2012;72:799–805. http://dx.doi.org/10.1016/j.compscitech.2012.02.007.
[31] Frishfelds V, Lundström TS. Modelling of particle deposition during impregnation of dual scale fabrics. Plast Rubber Compos 2011;40:65–9. http://dx.doi.org/10.1179/174328911X12988622800936.
[32] Lundström TS, Frishfelds V. Modeling filtration of particulate flow during impregnation of dual-scale fabrics. J Compos Mater 2012;47:1907–15. http://dx.doi.org/10.1177/0021998312452026.
[33] Hwang WR, Advani SG, Walsh S. Direct simulations of particle deposition and filtration in dual-scale porous media. Compos Part A Appl Sci Manuf 2011;42:1344–52. http://dx.doi.org/10.1016/j.compositesa.2011.05.017.
[34] Shih CH, Lee LJ. Tackification of textile fiber preforms in resin transfer molding. J Compos Mater 2001;35:1954–81. http://dx.doi.org/10.1177/002199801772661452.
[35] Rohatgi V, Lee LJ. Moldability of tackified fiber preforms in liquid composite molding. J Compos Mater 1997;31:720–44. http://dx.doi.org/10.1177/002199839703100705.
[36] Estrada G, Vieux-Pernon C, Advani SG. Experimental characterization of the influence of tackifier material on preform permeability. J Compos Mater 2002;36:2297–310. http://dx.doi.org/10.1106/002199802027542.
[37] Becker D, Mitschang P. Influence of preforming technology on the out-of-plane impregnation behavior of textiles. Compos Part A Appl Sci Manuf 2015;77:248–56. http://dx.doi.org/10.1016/j.compositesa.2015.05.001.
[38] Rimmel O, Becker D, Mitschang P. Maximizing the out-of-plane-permeability of preforms manufactured by dry fiber placement. Adv Manuf Polym Compos Sci 2016;2:93–102. http://dx.doi.org/10.1080/20550340.2016.1260900.
[39] Manfredi E, Michaud V. Packing and permeability properties of E-glass fibre reinforcements functionalised with capsules for self-healing applications. Compos Part A Appl Sci Manuf 2014;66:94–102. http://dx.doi.org/10.1016/j.compositesa.2014.07.006.
[40] Schindelin J, Arganda-Carreras I, Frise E, Kaynig V, Longair M, Pietzsch T, et al. Fiji: an open-source platform for biological-image analysis. Nat Methods 2012;9:676–82. http://dx.doi.org/10.1038/nmeth.2019.
[41] Meijering E. FeatureJ: An ImageJ Plugin Suite for Image Feature Extraction, <http://www.imagescience.org/meijering/software/featurej/>; 2003.
[42] Chalencon F, Orgéas L, Dumont PJJ, Foray G, Cavaillé JY, Maire E, et al. Lubricated compression and X-ray microtomography to analyse the rheology of a fibre-reinforced mortar. Rheol Acta 2010;49:221–35. http://dx.doi.org/10.1007/s00397-009-0393-5.
[43] Maire E, Colombo P, Adrien J, Babout L, Biasetto L. Characterization of the morphology of cellular ceramics by 3D image processing of X-ray tomography. J Eur Ceram Soc 2007;27:1973–81. http://dx.doi.org/10.1016/j.jeurceramsoc.2006.05.097.
[44] Rolland du Roscoat S, Decain M, Thibault X, Geindreau C, Bloch JF. Estimation of microstructural properties from synchrotron X-ray microtomography and determination of the REV in paper materials. Acta Mater 2007;55:2841–50. http://dx.doi.org/10.1016/j.actamat.2006.11.050.
[45] Koponen A, Kataja M, Timonen J. Permeability and effective porosity of porous media. Phys Rev E 1997;56:3319–25. http://dx.doi.org/10.1103/PhysRevE.56.3319.
[46] Williams JG, Morris CEM, Ennis BC. Liquid flow through aligned fiber beds. Polym Eng Sci 1974;14:413–9. http://dx.doi.org/10.1002/pen.760140603.
[47] Amico S, Lekakou C. Mathematical modelling of capillary micro-flow through woven fabrics. Compos Part A Appl Sci Manuf 2000;31:1331–44. http://dx.doi.org/10.1016/S1359-835X(00)00033-6.
[48] Gebart BR. Permeability of unidirectional reinforcements for RTM. J Compos Mater 1992;26:1100–33. http://dx.doi.org/10.1177/002199839202600802.
[49] Geodict. The Virtual Material Laboratory. Math2Market GmbH <www.geodict.com> [accessed 20 September 2016].
[50] Auriault J, Boutin C, Geindreau C. Homogenization of coupled phenomena in heterogenous media. John Wiley & Sons; 2010.
[51] Rolland du Roscoat S, Decain M, Geindreau C, Thibault X, Bloch J. Microstructural analysis of paper using synchrotron X-ray microtomography: numerical estimation of the permeability and effective thermal conductivity. Appita J J Tech Assoc Aust New Zeal Pulp Pap Ind 2008;61:286–90.
[52] Chalencon F, Dumont PJJ, Orgéas L, Foray G, Cavaillé JY, Maire E. Homogeneous and heterogeneous rheology and flow-induced microstructures of a fresh fiber-reinforced mortar. Cem Concr Res 2016;82:130–41. http://dx.doi.org/10.1016/j.cemconres.2015.12.012.
[53] Koivu V, Decain M, Geindreau C, Mattila K, Bloch J-F, Kataja M. Transport properties of heterogeneous materials. Combining computerised X-ray micro-tomography and direct numerical simulations. Int J Comput Fluid Dyn 2009;23:713–21. http://dx.doi.org/10.1080/10618561003727512.
[54] Kuentzer N, Simacek P, Advani SG, Walsh SM, Simacek P, Advani SG. Permeability characterization of dual scale fibrous porous media. Compos Part A Appl Sci Manuf 2006;37:2057–68. http://dx.doi.org/10.1016/j.compositesa.2005.12.005.
[55] Zhou F, Simacek P, Kuentzer N, Walsh SM, Advani SG. Analytic characterization of the permeability of dual-scale fibrous porous media. Compos Sci Technol 2006;66:2795–803. http://dx.doi.org/10.1016/j.compscitech.2006.02.025.
[56] Amico S, Lekakou C. An experimental study of the permeability and capillary pressure in resin-transfer moulding. Compos Sci Technol 2001;61:1945–59. http://dx.doi.org/10.1016/S0266-3538(01)00104-X.
[57] Michaud V, Mortensen A. Infiltration processing of fibre reinforced composites: governing phenomena. Compos - Part A Appl Sci Manuf 2001;32:981–96. http://dx.doi.org/10.1016/S1359-835X(01)00015-X.
[58] Wolfrath J, Michaud V, Modaressi A, Manson JA. Unsaturated flow in compressible fibre preforms. Compos Part A Appl Sci Manuf 2006;37:881–9. http://dx.doi.org/10.1016/j.compositesa.2005.01.008.
[59] Baranau V, Tallarek U. Random-close packing limits for monodisperse and polydisperse hard spheres. Soft Matter 2014;10:3826–41. http://dx.doi.org/10.1039/c3sm52959b.